© Indian Academy of Sciences

Sequence stratigraphy, depositional and diagenetic environments of the late Cambrian glauconite bearing oolitic limestones in the Kelan Section, Shanxi, China

Muhammad Riaz[1,2,3] ◉, G M Bhat[4,*], Khalid Latif[5] ◉, Tehseen Zafar[6,7] ◉ and Shahid Ghazi[7]

[1]*State Key Laboratory of Oil and Gas Reservoir Geology and Exploitation, Chengdu University of Technology, Chengdu 610059, China.*
[2]*College of Energy Resources, Chengdu University of Technology, Chengdu 610059, China.*
[3]*Centre for Geographical Information System, University of the Punjab, Lahore 54590, Pakistan.*
[4]*Department of Geology, University of Jammu, Gujarbasti, Jammu 180 006, Jammu and Kashmir, India.*
[5]*National Centre of Excellence in Geology, University of Peshawar, Peshawar 25130, Pakistan.*
[6]*Institute of Geochemistry, Chinese Academy of Sciences, Guiyang 550081, China.*
[7]*Institute of Geology, University of the Punjab, Lahore 54590, Pakistan.*
*Corresponding author. e-mail: bhatgm@jugaa.com

The current study presents results on depositional and diagenetic environments of the glauconite-bearing oolitic carbonates of the upper part of the basal third-order depositional sequence (DS_6) of the Cambrian Fengshan Formation at Kelan in the North China Platform. The Fengshan Formation comprises calcareous mudstone and shale of shelf environment followed by calcareous mudstone, micritic limestone of deep ramp to oolitic limestones of shallow ramp environments. The glauconite-bearing oolitic carbonates are restricted in the upper part of the sequence which was deposited during the forced regressive event. Petrographic study revealed that the sediments comprised of both carbonate and non-carbonate framework constituents. These constituents are mostly comprised of rounded to elliptical, radial-concentric ooids, dolomitized ooids, bioclasts (trilobites, brachiopod, and echinoderms), glauconitic pellets with fibro-radiating rims, and pyrite crystals. The radial-concentric structure of ooids suggests high-energy shallow water deposition conditions. Also, the presence of glauconite along with oolitic grainstone in the restricted upper portion of the Fengshan Formation provides credible evidence of its deposition under high-energy conditions during relative sea-level fall. It is therefore inferred that the glauconite was precipitated on or in close proximity to the Cambrian calcite seafloor during the forced regressive event prior to calcite cementation.

Keywords. Sequence stratigraphy; depositional environment; glauconite; ooids; Cambrian Fengshan Formation; North China platform.

1. Introduction

Cambrian carbonate platforms are widespread low gradient ramps or rimmed shelves that formed during warm climate periods within typical calcite seas (Balthasar and Cusack 2015) during sea-level highstand (Miller *et al.* 2005; Haq and Schutter 2008). The shallowing upward cycles are the basic building blocks of shallow carbonate platform successions (Fürsich *et al.* 2005; Tucker and Garland 2010; Xiao *et al.* 2021a). The analysis of the cyclic stacking pattern is accordingly crucial for the identification of depositional sequences, component systems tracts, and sequence boundaries on the broad carbonate platform (Schlager 2005).

The late Cambrian is an important geological period that can be categorized on the basis of specific stratigraphic and sedimentological features such as: (1) the highest position of sea-level (Haq and Schutter 2008); (2) lack of reef-framework metazoan builders (Rowland and Shapiro 2002; Kiessling 2009; Cordiea *et al.* 2019); (3) dominance of trilobites (Peng *et al.* 2012; Babcock *et al.* 2016); (4) skeleton-poor sea dominated by storms (Pratt and Bordonar 2007; Pruss *et al.* 2010); (5) period of an increase of atmospheric O_2 (Husson and Peters 2017; Laakso and Schrag 2017) as well as a widespread euxinia (Gill *et al.* 2011) or persistent oceanic anoxia (Saltzman *et al.* 2015). Under these conditions, a special pattern of late Cambrian carbonates developed around the globe which comprises of the following features: (1) carbonate platform dominated by lime muds which are genetically related to microbial activities (Pratt *et al.* 2012); (2) high abundance of microbial carbonates especially for thrombolite and dendrolite (Riding 2000, 2011a, b); and (3) microbial carbonates dominated by an abundance of fossils of calcified sheaths of cyanobacteria (Lee and Riding 2018; Xiao *et al.* 2018, 2020a; Latif *et al.* 2019; Mei *et al.* 2020a, b, 2021).

The Cambrian platforms developed under these conditions include those of North America, Australia, Europe, Asia, Middle East, and Siberia (Riaz *et al.* 2019a and references therein). North China Platform (NCP) is one of such examples which provides an excellent case history of how carbonate deposition responded to long-term changes in the relative sea-level and the environment, largely brought about by changes in the regional geotectonic regime and tectonic eustasy (Meng *et al.* 1997; Myrow *et al.* 2015). The late Cambrian (Furongian) strata at Kelan Section,

Shanxi Province of the NCP comprises of the Changshan and the Fengshan formations, which are coeval with the Chaomidian Formation (see Chen *et al.* 2014; Lee *et al.* 2014; Riaz *et al.* 2019b). These formations comprise three third-order depositional sequences which are bounded by drowning unconformities similar to other sections of the NCP as described by Latif *et al.* (2018) and Riaz *et al.* (2019a, b). Contrary to other sections of the NCP, the Furongian strata at the studied section contain glauconite-bearing oolitic limestone, mostly lime mud which makes this section unique from the other sections of the NCP. Recently, Riaz *et al.* (2019a) comprehensively described the sequence stratigraphy of the entire Cambrian strata of the same section but did not highlight the non-carbonate constituent (glauconite) in the Furongian strata. Globally, several researchers have ascribed the depositional environment of glauconite formation to condensed section (CS), transgressive systems tract (TST), highstand systems tract (HST), and lowstand systems tract (LST) (e.g., Chen 1994; Amorosi 1995, 1997, 2012; Morad *et al.* 2000; Banerjee *et al.* 2008). However, the presence of glauconite along with ooids in the restricted portion of the formation during relative sea-level fall, i.e., forced regressive systems tract (FRST) is hitherto unknown. The present work provides shreds of evidence regarding the deposition of glauconite bearing ooids during relative sea-level fall and fits well with the Schlager (2005) model of sequence stratigraphy and negates the standard model of sequence stratigraphy (Catuneanu *et al.* 2011) wherein an erosional unconformity is postulated to develop during relative sea-level fall.

2. Study area

The 'Kelan Section' is located in the west of Luya Mountain, northwest of Shanxi Province, and middle of Cambro-Ordovician North China Platform (figure 1a–b; Riaz *et al.* 2019a). The North China Platform is a vast epeiric platform that extends over an area of 1000 km from north to south, and 1500 km from east to west (figure 1a) (Myrow *et al.* 2015; Riaz *et al.* 2019b). The palaeogeographic reconstruction shows this platform as a part of the Sino-Korean plate, which was situated in the northern Gondwana continent adjacent to Australia (Wotte *et al.* 2007). After the break-up of the supercontinent Rodinia, the North
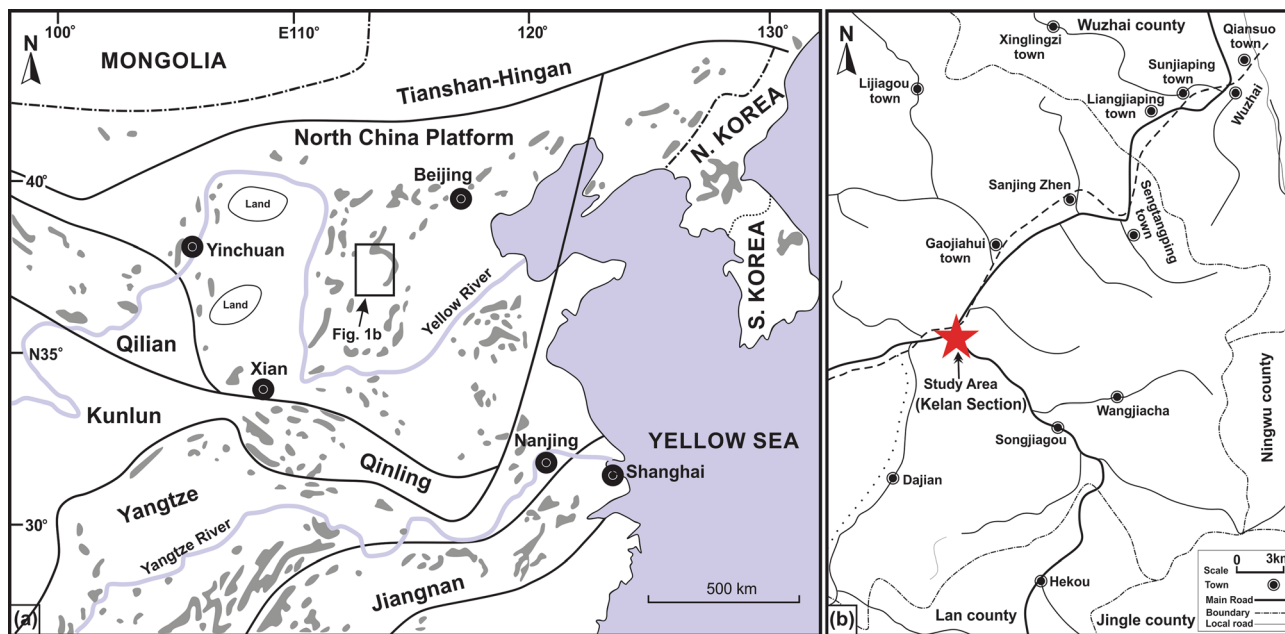
Figure 1. (**a**) Geological framework of the North China Platform (modified after Myrow *et al.* 2015; Riaz *et al.* 2019a). Gray areas comprise Cambrian–Ordovician outcrops. The text 'Land' in circles reveals late Cambrian exposed areas on the western side of the North China Platform. The rectangle shows the study area. (**b**) The red star represents the location of the Kelan Section.

China Platform started to subside (Meng *et al.* 1997) and received sediment influx during mid-late lower Cambrian (middle Terreneuvian) transgression which was restricted to the eastern, western, and southern margins of the platform (Latif *et al.* 2018). During the long-term sea-level rise, approximately 700 m thick strata of Cambrian sediments were deposited in this epeiric basin (Kwon *et al.* 2006) comprising of dolostone and limestone in the lower Cambrian; oolitic grainstone in the middle Cambrian and carbonate mud in the upper Cambrian (Mei *et al.* 2020a; Riaz *et al.* 2020). The outcrops of the current study occur about 15 km away from the Kelan city (at 38°44′41″N, 111°34′45″E) and extend from southeast to southwest (figure 1b) (Riaz *et al.* 2019a).

3. Materials and methods

We studied and measured a 106-m thick section of Fengshan Formation at Kelan and marked its upper and lower boundaries. Here, the Fengshan Formation overlies the Furongian carbonates of Changshan Formation and underlies the Yeli Formation of the lower Ordovician age. The sedimentary structures including edgewise conglomerates were observed in the lower part of the formation and the glauconite-bearing oolitic carbonates were observed

in its upper part. The 31 random samples were collected from the Fengshan Formation. Out of them, 10 samples were taken from a targeted portion of glauconite-bearing oolitic limestone. One sample was taken from the upper part of the Cambrian Changshan Formation and one from the lower part of the Ordovician Yeli Formation. Details of the section measurements and other field observations including lithofacies, sedimentary structures meter-scale sedimentary cycles, etc., are presented in figure 2. The oriented thin sections were prepared from the collected samples and were studied under a high magnification microscope at the China University of Geosciences, Beijing. Detailed petrographic analyses were carried out under Zeiss Axio Scope A1 microscope to study the fabric, structure, and composition of the ooids and glauconite along with other carbonate and non-carbonate constituents to decipher their depositional and diagenetic history. Photomicrographs were taken at different magnifications for documentation of the characteristics of carbonate and non-carbonate components in the thin sections. The X-ray diffraction (XRD) analysis was carried out on six powder samples (table 1) from the targeted beds (figure 2) to determine the mineralogy of these rocks. The XRD analysis was performed by using the Bruker D2 PHASER instrument. Calcite was taken as the reference standard mineral to
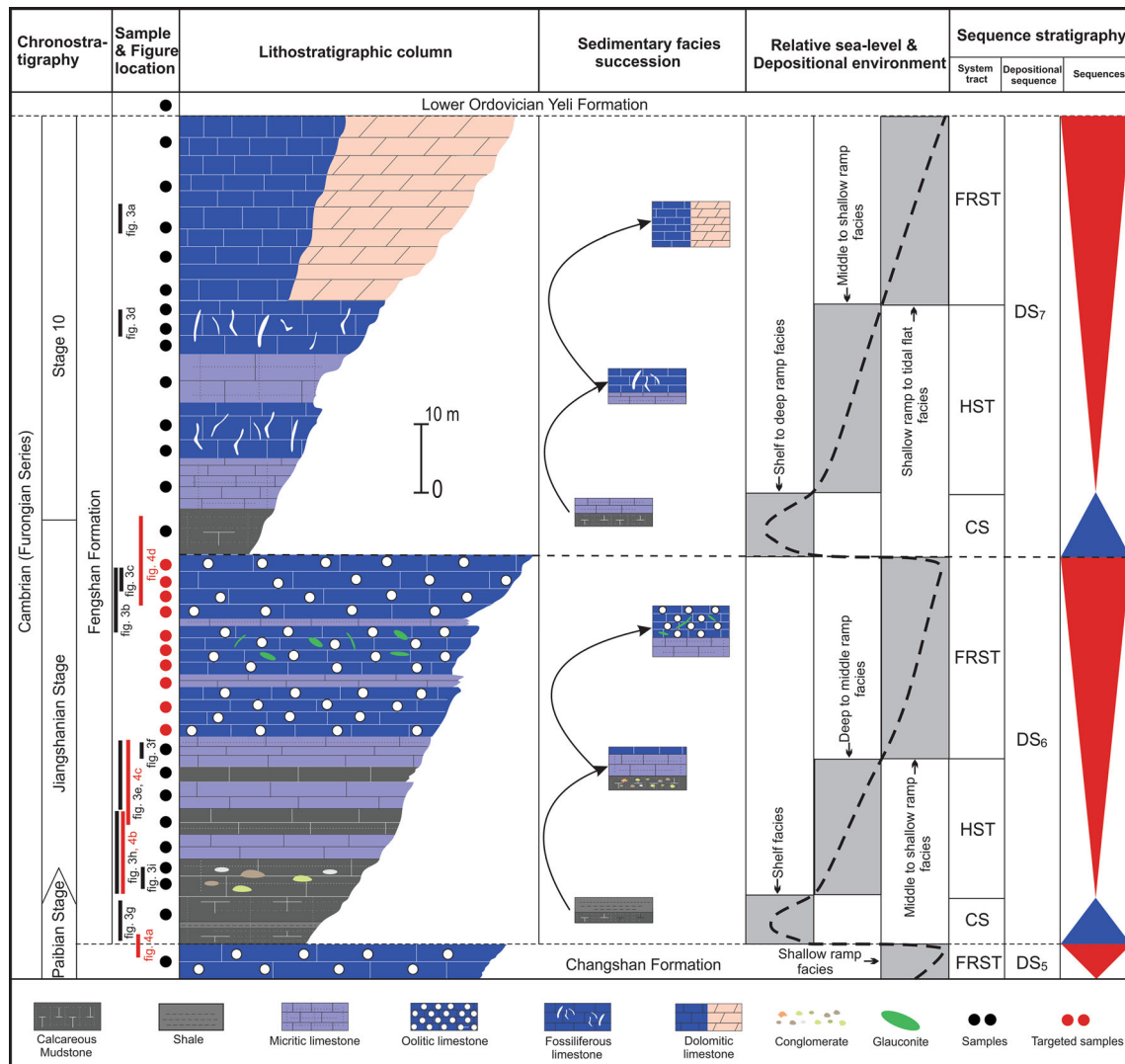
Figure 2. Sequence stratigraphic column of the Cambrian (Furongian) Fengshan Formation (DS$_6$–DS$_7$) revealing a general shallowing upwards pattern of sedimentary facies. FRST: forced-regressive systems tract; HST: highstand systems tract; CS: condensed section; DS: depositional sequence.

Table 1. *XRD analysis portraying the percentage of minerals in the samples of the upper part of the basal third-order sequence (DS$_6$).*

Sl. no.	Sample no.	Mineral Composition Content (%) of XRD quantitative					
		Calcite	Dolomite	Quartz	K-Feldspar	Pyrite	Clay mineral
1	FS-13	82	10	3	2	1	2
2	FS-14	89	5	2	0	1	3
3	FS-16	81	9	3	2	2	3
4	FS-17	86	7	5	0	0	2
5	FS-18	92	3	2	0	2	1
6	FS-19	79	12	3	1	1	4

determine the entire mineral composition of the rock samples. Its value was set as (RIP$_{reference}$: $I_{reference}$/ $I_{Calcite}$: 1). The volume percentage of each mineral was calculated by using the determined XRD weight percentage and density (Al-Jaroudi *et al.* 2007):

$$V_i = \frac{100(W_i/\rho_i)}{(W_a/\rho_a) + (W_c/\rho_c) + (W_d/\rho_d) + (W_q/\rho_q)}$$

where V_i is the vol.% of anhydrite, calcite, dolomite, and quartz; W_i and ρ_i are their corresponding

wt.% and grain densities, respectively. The subscripts *a*, *c*, *d*, and *q* refer to the phases anhydrite, calcite, dolomite, and quartz, respectively.

Furthermore, a scanning electron microscope (SEM) study was carried out on five representative polished thin sections to determine the elemental composition of the pellets. These thin sections were studied under an FEI Quanta 200F scanning electron microscope. The thin sections were gold-coated for secondary electron imaging. Semi-quantitative element analyses of sub-micron-sized spots during SEM observations were obtained using energy-dispersive X-ray spectroscopy (EDX) under a high voltage of 10.0 kV. The current pulse ranged from 19.83 to 42.58 kcps. Also, energy-dispersive X-ray detection (EDX) analysis was performed to identify glauconite, whereas the calcitic composition of ooids was cross-checked by XRD analysis. The geochemical analyses were performed in the State Key Laboratory of Oil and Gas Geology and Exploitation, Chengdu University of Technology, China.

4. Lithofacies of the Fengshan Formation

Sedimentary facies of the Fengshan Formation based on field observations were categorized into: (1) dolomitic limestone facies; (2) oolitic limestone–micritic limestone heterolithic facies; (3) micritic limestone–fossiliferous limestone heterolithic facies; (4) calcareous mudstone–thick bedded micritic limestone heterolithic facies; (5) calcareous mudstone–thin bedded micritic limestone heterolithic facies; and (6) calcareous mudstone–shale heterolithic facies. The detailed account of each facies and their stacking pattern is presented as depositional facies here.

4.1 *Back ramp facies*

4.1.1 *Dolomitic limestone facies (L-1)*

Description: This facies is 10 m thick and comprises medium to thick-bedded light gray dolomitic limestone (figure 3a) which forms a peritidal type M-cycle. Dolomitic limestone contains few small cavities and gives a weak reaction to dilute acid. It forms the upper part of the formation where it marks upper contact with the lower Ordovician Yeli Formation.

Interpretation: Few cavities in dolomitic limestone indicate the shrinkage that occurred during the conversion of calcite into dolomite (Abdulghania *et al.*

2020). The weak reaction with dilute acid indicates some contents of calcite (Jafarian *et al.* 2018; Abdulghania *et al.* 2020). Dolomitic limestone is the tidal flat facies that are deposited above the fair weather wave base (Jafarian *et al.* 2017, 2018). This facies was deposited during relative sea-level fall and formed a forced regressive system tract (FRST).

4.2 *Shallow ramp facies*

4.2.1 *Oolitic limestone–thin micritic limestone heterolithic facies (L-2)*

Description: This lithofacies is 25 m thick and comprises light yellow oolitic limestone and light gray micritic limestone (figure 3b). This heterolithic facies fizzes with acid. Micritic limestone is fine-grained, whereas oolitic limestone is medium sand size (figure 3c). Oolitic limestone is well compacted and cemented by calcite. Small hairline white veins run through this rock. A few biogenic fragments are also observed. Field observations show an interbedding of medium- to thick-bedded oolitic limestone and thick- to thin-bedded micritic limestone (figure 3b). Subtidal meter-scale cycles are also observed in this lithofacies.

Interpretation: This heterolithic facies formed subtidal meter-scale cycles that indicate the deposition of thin-bedded micritic limestone during the rise of sea-level at a very small scale (e.g., Mei *et al.* 2005; Latif *et al.* 2018). Whereas thick-bedded oolitic limestone depicts the sedimentation during sea-level fall within a small cycle (Mei *et al.* 2005; Riaz *et al.* 2019a). Oolitic limestone is deposited in moderate to high-energy marine environments (Flügel 2004). Micritic limestone with oolitic limestone depicts the high energy environment with intervals of quiescence (Riaz *et al.* 2019a, 2021; Xiao *et al.* 2020b, 2021a). This heterolithic facies is interpreted to have formed in high-energy environment during the late highstand systems tract (LHST) of the third-order depositional sequence similar to the Miaolingian strata of the North China Platform (Riaz *et al.* 2019a).

4.3 *Middle to deep ramp transitional facies*

4.3.1 *Micritic limestone–fossiliferous limestone heterolithic facies (L-3)*

Description: This facies comprises thick to thin-bedded micritic limestone and thin to thick-bedded
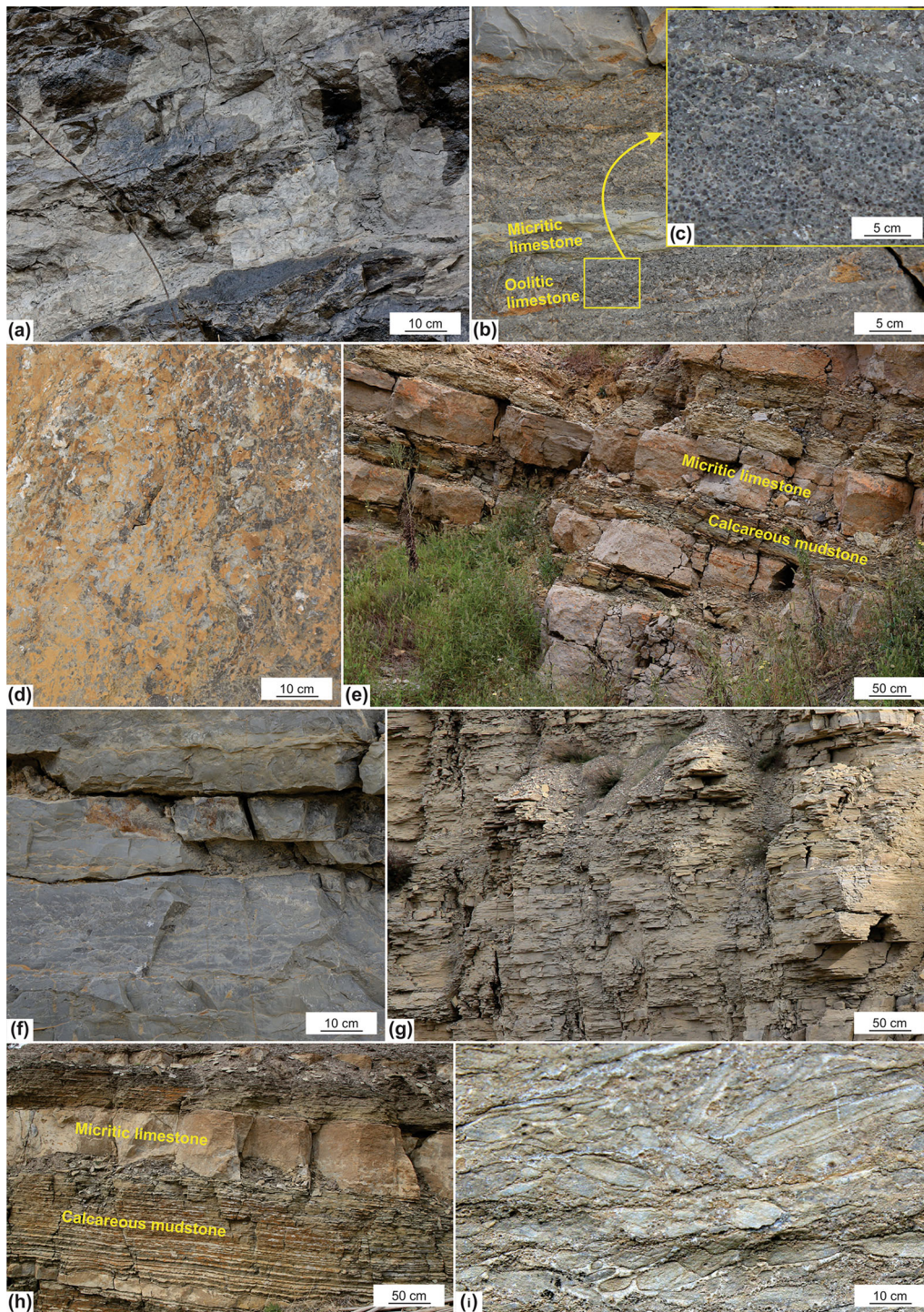
Figure 3. Meso- and macroscopic photographs of the heterolithic facies of the Fengshan Formation at Kelan Section. (**a**) Dolomitic limestone forms tidal flat facies, (**b**) oolitic limestone–thin micritic limestone heterolithic form shallow ramp facies, (**c**) oolitic limestone in shallow ramp facies, (**d**) fossiliferous limestone, (**e**) medium to thick micritic limestone and thin-bedded calcareous mudstone in middle ramp facies, (**f**) medium to thick micritic limestone in middle ramp facies, (**g**) heterolithic calcareous mudstone and shale of the shelf facies form the lower part of the Fengshan Formation, (**h**) heterolithic facies 'thick calcareous mudstone–medium to thin micritic limestone' formed deep ramp facies, and (**i**) edgewise conglomerate within calcareous mudstone in deep ramp facies.

fossiliferous limestone. This facies is 25 m thick and formed tide type M-cycle. The fossiliferous limestone has weathered to a pale yellow-gray. The

bedding thickness of micritic limestone decreases upward, whereas it increases in the case of fossiliferous limestone. No fossils were observed in the

micritic limestone in contrast to the fossiliferous limestones (figure 3d).

Interpretation: Thick to thin bedding of fine-grained micritic limestone shows the transition from deep to middle ramp setting (Meng *et al.* 1997). Whereas thin to thick beds of the fossiliferous limestones depict relatively high energy settings as compared to the micritic limestones (Riaz *et al.* 2019a). However, fossiliferous limestone also shows the transition from middle to shallow ramp setting. This entire heterolithic facies reflects deposition in the middle ramp setting.

4.3.2 *Calcareous mudstone–thick bedded micritic limestone heterolithic facies (L-4)*

Description: This heterolithic facies is 15 m thick and comprises yellowish-gray calcareous mudstone and dark gray micritic limestone (figure 3e). The calcareous mudstone is thin-bedded, while micritic limestone is thick-bedded. The dark gray micritic limestone is brittle and breaks with a conchoidal structure (figure 3f). This facies forms subtidal meter-scale cycles (figure 3e).

Interpretation: The calcareous mudstone is thin-bedded, whereas micritic limestone is thick-bedded. It indicates the deposition of calcareous mudstone and micritic limestone in relatively deeper than L-3 facies. This heterolithic facies (L-4) reflects the transition from deep to middle ramp setting and formed middle highstand systems tract (MHST) of the third-order depositional sequence.

4.4 *Deep ramp facies*

4.4.1 *Calcareous mudstone–shale heterolithic facies (L-5)*

Description: This heterolithic facies is 5 m thick and comprises calcareous mudstone and shale (figure 3g). The calcareous mudstone is yellowish-gray, whereas the shale is dark gray. The calcareous mudstone is fine-grained and comprises fine-scale laminations (figure 3g). The shale is fine-grained and distinguishes it from calcareous mudstones due to its laminations (figure 3g). This facies occurs in the lower part of the formation and makes conformable lower contact with the oolitic limestone in the upper part of the Changshan Formation.

Interpretation: The fine-grained calcareous mudstone and shale indicate the low energy environment (Flügel 2010; Riaz *et al.* 2019b). Calcareous mudstone–shale heterolithic facies belong to deep ramp setting and formed condensed section of the basal third-order depositional sequence (see Mei *et al.* 1997; Xiao *et al.* 2021a).

4.4.2 *Calcareous mudstone–thin bedded micritic limestone heterolithic facies (L-6)*

Description: The lithofacies is 10 m thick and consists of yellowish-gray calcareous mudstone and yellow to gray micritic limestone. Micritic limestone is dense, uniform, fine-grained, and breaks with a conchoidal fracture. The bedding thickness of this facies gradually changes from the lower to the upper part of the formation (figure 3h). The facies form L-M type meter-scale cycles (figure 3h). The yellowish-cream edgewise conglomerates are also observed within calcareous mudstone (figure 3i). These conglomerates are poorly sorted, and possess iron encrustation around them.

Interpretation: Calcareous mudstone indicates a low-energy environment (Flügel 2010). Micritic limestone with calcareous mudstone also depicts the low-energy environment (Flügel 2010; Jafarian *et al.* 2017). This heterolithic facies was deposited in a deep ramp setting during early highstand systems tract (EHST). Edgewise conglomerates are similar to the intraclastic flat-pebble conglomerates of Whisonant (1987) from the upper Cambrian strata in Virginia. These conglomerates indicate a severe storm event. Moreover, L-M cycle indicates the fluctuation of relative sea-level on small scale.

5. Sequence stratigraphy

The sequence boundaries of the Furongian strata at the studied section are marked by facies change from shallow to deep ramp facies (oolitic limestone to calcareous mudstone) (figure 4). The Fengshan Formation comprises two third-order depositional sequences (DS_6 and DS_7) (figure 2). The basal part of the depositional sequence DS_6 (figures 2, 4a) of the Fengshan Formation comprises 5 m thick heterolithic deep ramp facies of calcareous mudstone and shale (figure 3g). This facies was deposited during relative sea-level rise i.e., transgressive systems tract (TST), and makes condensed section

(CS) of the first depositional sequence DS_6 (figures 2, 3g, 4a, 5). The HST of DS_6 is also comprised of massive calcareous mudstone and thick micritic limestone of deep ramp facies (figures 3h, 5). This deep ramp facies form L-M type meter-scale cycles (figures 4b, 5). The deep to middle ramp facies is also the result of HST that deposited calcareous mudstone and thick beds of micritic limestone in the middle part of the depositional sequence (DS_6) (figures 2, 3e, 4c). The shallow ramp facies are composed of thin-bedded micritic limestone interbedded with thick oolitic limestone along with patches of glauconite and form the upper part of the depositional sequence DS_6 (figures 2, 3b–c). The oolitic limestone of shallow ramp facies was deposited during the relative sea-level fall during forced regressive wedge systems tract (FRWST) as proposed by Hunt and Tucker (1992), Mei and Yang (2000), Mei (2010), and Samanta *et al.* (2016) elsewhere, which is equivalent to the falling-stage systems tract

(FSST) of Nummedal *et al.* (1995), and Schlager and Warrlich (2009), and the late-highstand systems tract (LHST) of Mei (2015) (figures 4d, 5). The middle to shallow ramp sequences are comprised of subtidal meter-scale cycles (figures 4c, 5). After that, second third-order depositional sequence (DS_7) of the Fengshan Formation was deposited in which deep ramp facies comprised of calcareous mudstone and micritic limestone forming the condensed section (CS) of the depositional sequence DS_7 (figures 2, 4d, 5). This sequence overlies the oolitic limestone of shallow ramp facies of the depositional sequence DS_6 (figure 4d). The middle and shallow ramp facies formed a 25-m thick sequence during HST which is composed of thinly bedded micritic limestone and thin to thick-bedded fossiliferous limestone forming tidal type M-cycle pattern (figure 2). The shallow ramp to tidal flat 25-m thick sequence of dolomitic limestone is formed during the relative sea-level fall, i.e., forced regressive systems tract (FRST)
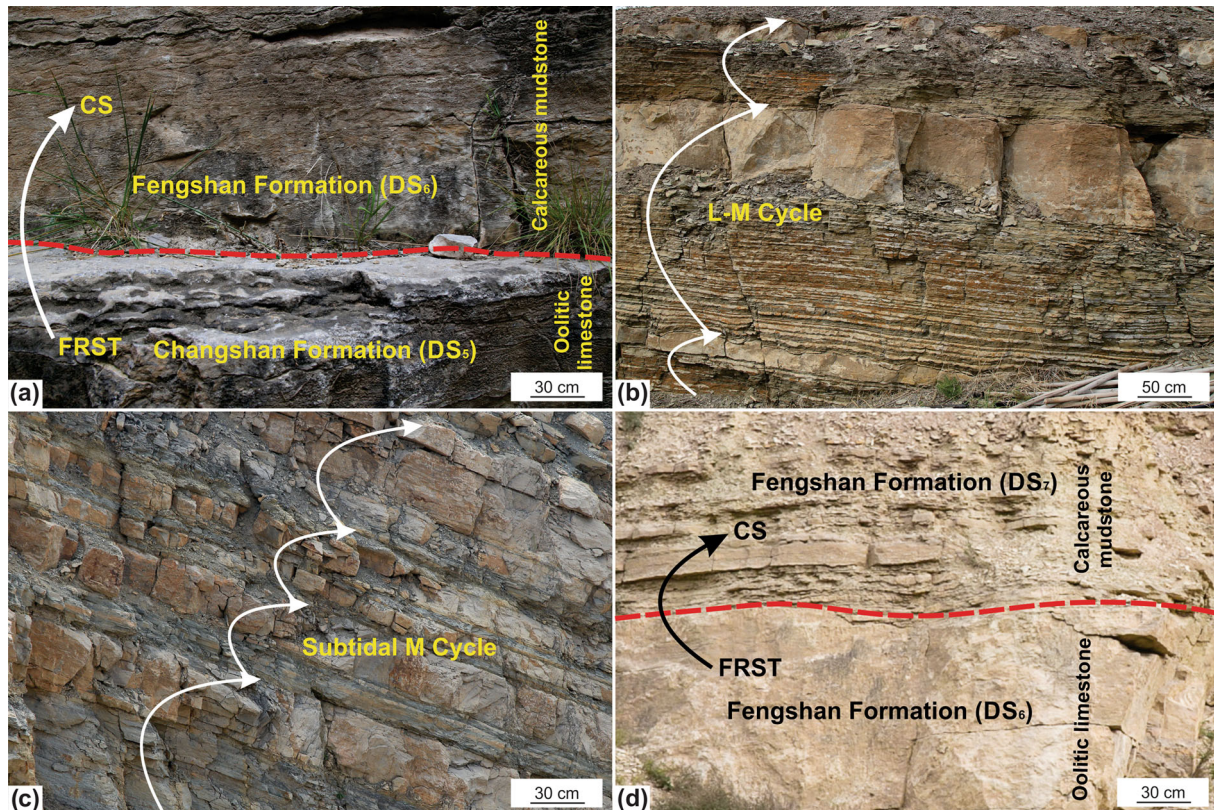

Figure 4. (**a**) The boundary between oolitic limestone of the Changshan Formation and calcareous mudstone of the basal third-order depositional sequence of the Fengshan Formation show the drowning unconformity, (**b**) L-M meter cycle deposited during deep ramp setting in the basal third-order depositional sequence, (**c**) subtidal type M-cycle deposited in middle ramp setting, (**d**) the boundary between glauconite bearing oolitic limestone of shallow ramp facies in the upper part of the basal third-order depositional sequence of the Fengshan Formation and calcareous mudstone of shelf facies in the lower part of the upper third-order depositional sequence of the Furongian Formation indicate the Type-3 drowning unconformity.
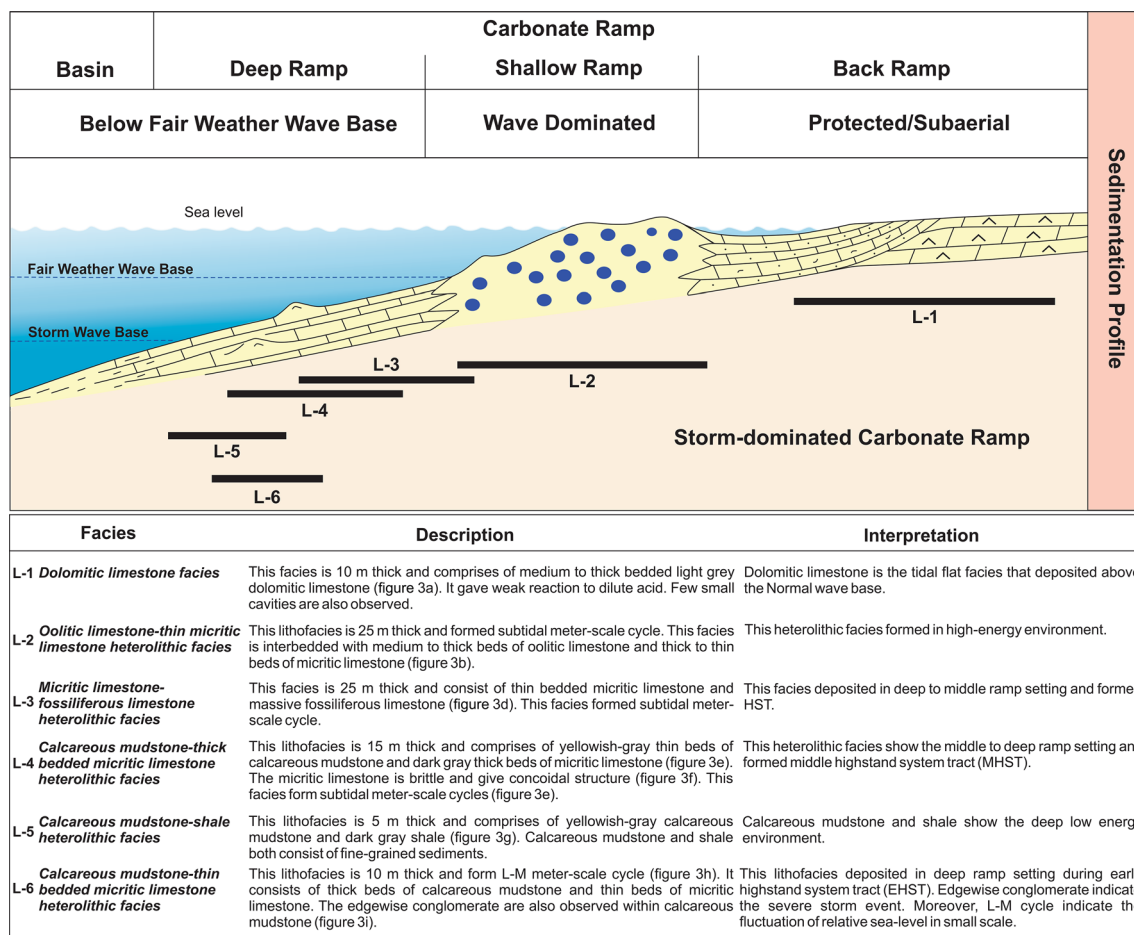
Figure 5. Schematic diagram of ramp-type setting (modified after Meng *et al.* 1997) showing the sedimentary facies recognized within the Fengshan Formation, Kelan Section.

(figures 2, 3a). Dolomitic limestone makes conformable upper contact with the lower Ordovician Yeli Formation (figure 2).

6. Mineralogy and geochemistry

6.1 *XRD analysis*

Calcite in all the six analyzed samples is a dominant component (table 1) of the upper part of the basal third-order sequence which comprises oolitic limestone. These samples contain 79, 92, 86, 81, 89 and 82% calcite with a mean of 85% (table 1). The second abundant mineral found in these samples is dolomite with a maximum in FS-19 (i.e., 12%) and minimum in FS-18 (i.e., 3%). The content of dolomite in these six samples is 12, 3, 7, 9, 5 and 10% with a mean of 7.5% (table 1). Quartz is the third major mineral observed in these samples with a range of 2–5% (mean value 3%) (table 1). The other minerals, i.e., kaolinite, potash feldspar, and

pyrite were observed in minor amounts. Clay minerals are maximum in FS-19, i.e., 4%, and minimum in FS-18, i.e., 1%, and found the same proportions in the remaining samples but pyrite mineral is less in proportion and has no observable consistency. Potash feldspar is only observed in three samples, i.e., FS-19, FS-16, and FS-13 with 1, 2, and 2%, respectively (table 1).

6.2 *SEM and EDX analysis*

SEM and EDX were used to determine the non-carbonate constituents particularly glauconite pellets in the samples from the DS_6 sequence. SEM photographs show the presence of oolitic grainstone where the individual sizes of ooids range from 0.5 to 1 mm (figure 6a). Further, observation shows the cross-section view of the ooids that consist of tiny crystals of calcite which ranges in size from 0.02 to 0.04 mm (figure 6a, b). Moreover, mould structures in the surrounding area of the ooids are

also observed in the SEM analysis (figure 6a). Some of the samples were also scanned in SEM to study the morphology of major minerals present in pellets (figure 6c–c′ and d–d′). From this SEM photomicrograph, it is evident that the mineral glauconite is present in irregularly shaped patches (spots marked as EDX001 and EDX002). These spots were analyzed by EDX to ascertain the presence of glauconite. The EDX analyses of the marked patches are shown in figure 6(c–c′). The EDX analysis of the marked patches shows the presence of Si, K, Al, Mg, O, and Fe, all the essential constituents of glauconite (figure 6d–d′).

7. Petrographic types

The restricted upper portion of the Fengshan Formation (DS_6) is mainly composed of ooids, glauconite pellets, and pyrite minerals, along with minor amounts of bioclasts including fragments of trilobites and brachiopods (figure 7a–c). Among the carbonate framework constituents, ooids are most common while the most common non-carbonate constituents include glauconite pellets and a minor amount of pyrite (figure 7a–c). A detailed description of each constituent is given below.

7.1 *Carbonate components*

Ooids and bioclasts are the major carbonate constituents observed in thin sections of the DS_6 depositional sequence (figures 7a, 8). Ooids are mostly rounded with diameters ranging from 0.25 to 2.00 mm and categorized into radial-concentric ooids, and dolomitized ooids, which are dominating constituents in the upper part of the DS_6 sequence (figures 2, 3b–c, 8a–e). Among the ooid-bearing grainstones, radial-concentric ooids are rounded in shape and their nuclei mostly comprise detrital grains or skeletal fragments enveloped either by one or more concentric layers or by composite concentric-radial ring structure (figure 8a–c). Microboring is also observed particularly in the cortex of radial-concentric ooids (figure 8a–c). The dolomitized ooids are associated with tiny crystals of dolomite (figure 8a, b, d, e). Moreover, these dolomitized ooids are classified into partially dolomitized ooids (figure 8d) and completely dolomitized (figure 8e). Further observation shows the bioclasts include either broken pieces of

trilobite or brachiopods (figures 7a, 8f) as their nuclei. An echinoderm fossil is also observed in the thin section (figure 8f). These ooids are mainly cemented by sparite (figure 8a–e), however, micrite is also observed in few ooids (figure 8a, f).

7.2 *Non-carbonate components*

Glauconite and pyrite minerals are the major non-carbonate constituents found in the DS_6 depositional sequence (figure 9a–i). Glauconite is cemented by sparite and found in the surrounding area of ooids (figure 9a–g). Glauconites mainly occur as pellets (figure 9a–e) and fibro-radiated rims (figure 9f). These pellets of glauconite are green and range in size from fine sand to fine silt (150–400 µm). These pellets have relatively larger sizes than micritic patches, with a smooth to wrinkled surface texture (figure 9a). The substrates of the pellets are thoroughly altered and there is no evidence to correlate it to any precursor (figure 9a). Such types of glauconitic pellets are called Type 1 (Banerjee *et al.* 2015). The fibro-radiated rims either partially or completely covered the grains (figures 7b–c, 9f). Glauconite is also observed in fractures in the form of bands (figure 9g). The dolomitized ooids and glauconitic pellets are bounded by fibro-radiating rims of micrite (figures 7b, 9b–f). Pyrite is the second major non-carbonate constituent of the analyzed samples found in ooid-bearing grainstones (figure 9c–d, h–i). The size of these pyrite crystals varies from 0.04 to 0.2 mm (figure 9h–i).

8. Discussion

The Furongian Fengshan Formation at Kelan Section of the North China Platform comprises two third-order sequences (figure 2). The depositional style of the basal third-order depositional sequence (DS_6) which grades upward from calcareous mudstone of deep ramp facies to the oolitic limestone facies of shallow ramp displays shallowing upward sequence (figures 2, 3). The lower contact of DS_6 is an abrupt transition from the oolitic-grain bank of the Changshan Formation to the calcareous mudstone of the basal third-order depositional sequence (DS_6) (figure 4a). Its upper contact with the calcareous mudstone of the deep ramp facies in the lower part of the upper third-order depositional sequence (DS_7) of the Fengshan Formation is gradational (figure 4d). Both these boundaries
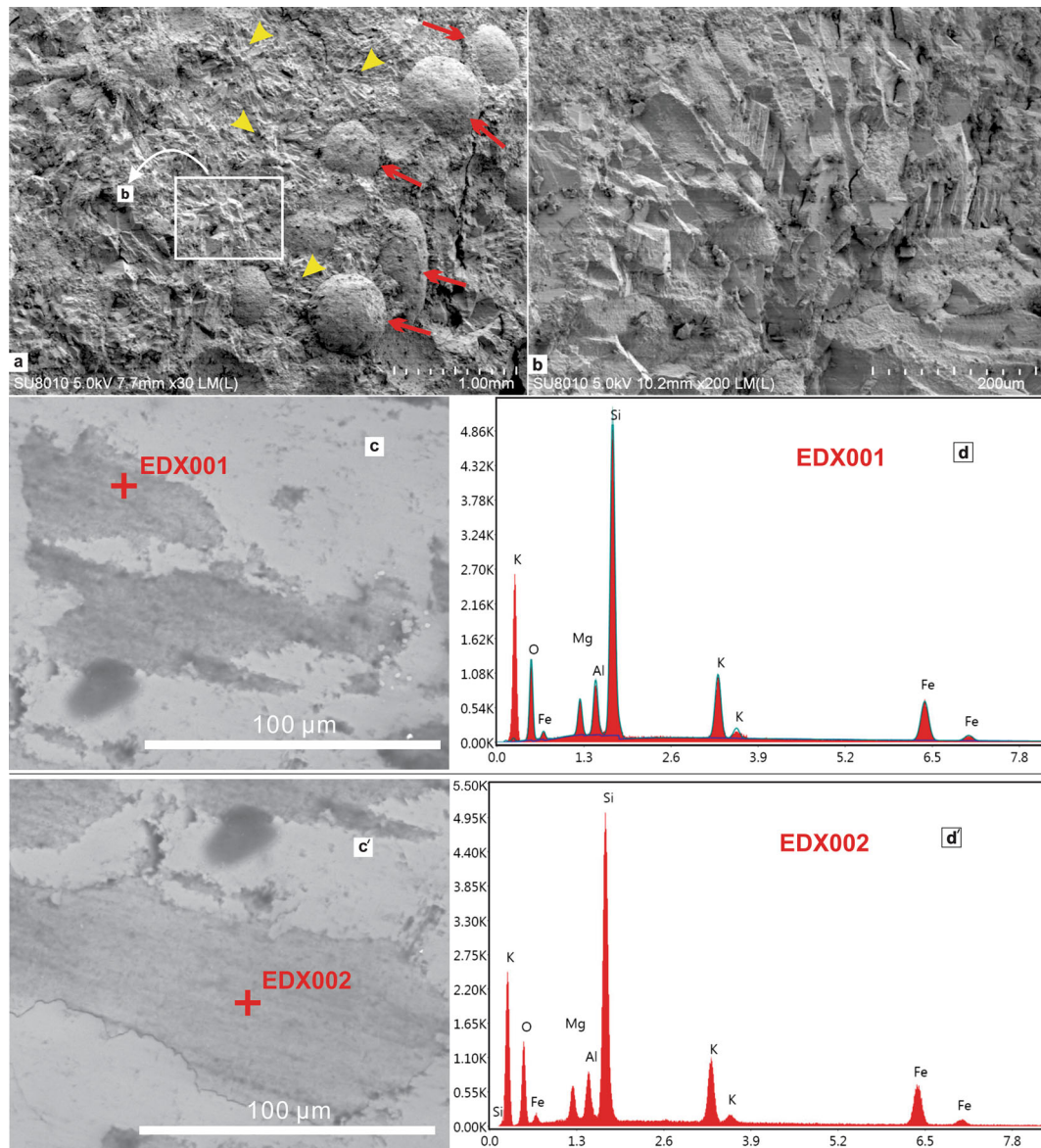
Figure 6. SEM and EDX analysis of the carbonate and non-carbonate constituents in the upper part of the basal Fengshan Formation (DS$_6$). (**a**) Displays the presence of oolitic grainstone (red arrow) and crystals of calcite (yellow arrowhead). Rectangle shows the enlarged part of calcite crystals in photo b, (**b**) SEM photograph indicates the crystals of calcite, (**c–c′**) show the pellets of the glauconite with the point of EDX analysis marked, and (**d–d′**) EDX results confirm the composition of glauconite.

represent typical drowning events (figure 4a, d) that developed during the rapid rise of relative sea-level (e.g., Schlager 1999). The upper third-order depositional sequence DS$_7$ shows facies variation from deep ramp facies (calcareous mudstone) to tidal flat facies (dolomitic limestone) (figures 2, 5). The facies lower boundary of the upper third-order depositional sequence possibly represents the drowning unconformity type sequence boundary, whereas its upper contact with Ordovician sediments (Yeli Formation) is a typical exposure discontinuity, which represents the Type 1 sequence boundary of the Exxon model (i.e., Vail *et al.* 1977).

Macroscopic characteristics show the calcareous mudstone (figures 2, 3g), and heterolithic thin micritic limestone and thick calcareous mudstone of deep ramp facies (figures 2, 3h) exhibit the relative sea-level rise. Whereas glauconite-bearing oolitic limestone of the shallow ramp facies depicts the relative sea-level fall (figures 2, 3b–c). These regressive deposits were covered by calcareous mudstone and micritic limestone of deep ramp facies which also indicate the relative sea-level rise (figure 2). Gradually, tidal-flat dolomitic limestone formed with relative sea-level fall (figure 3a). Consequently, Furongian Fengshan Formation formed two
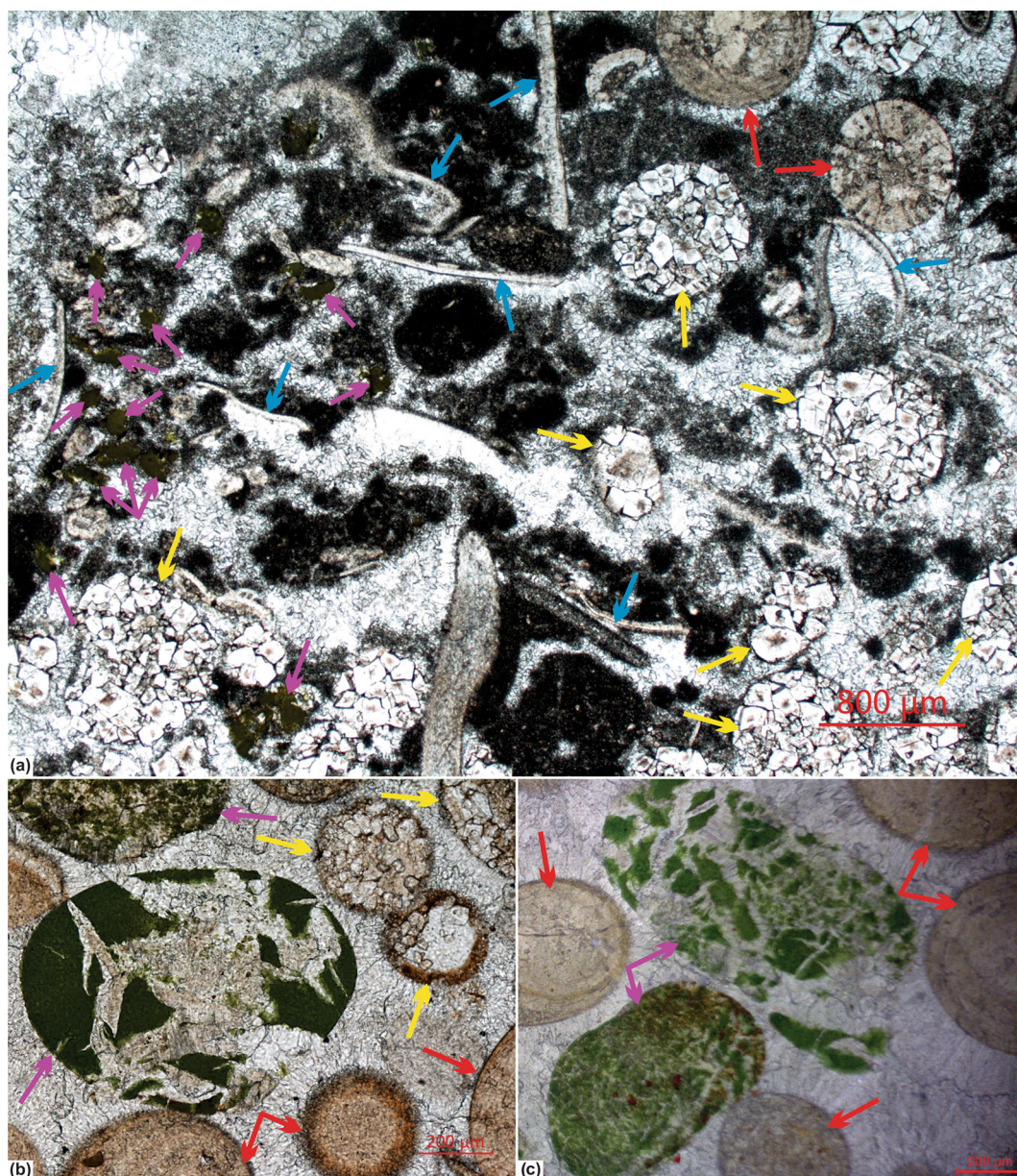
Figure 7. Photomicrographs show the carbonate and non-carbonate constituents in the upper part of the basal Fengshan Formation. (**a**) Glauconite (pink arrows), radial concentric ooids (red arrows), dolomitized ooids (yellow arrows), brachiopods and trilobites (blue arrows), (**b–c**) radial-concentric ooids without core (red arrows), dolomitized ooids (yellow arrows), and pellets of glauconite mineral (pink arrows) are cemented by sparite.

third-order depositional sequences at the studied section similar to the other sections of the North China Platform (Xiao *et al.* 2017a, b; Latif *et al.* 2018, 2019; Riaz *et al.* 2019a, b). The top parts of each subsequence in other sections of the North China Platform are associated with biohermal limestone and dolomitic limestone, respectively, such as the Qijiayu Section (Hebei) (Xiao *et al.* 2017a, 2020a), Cangerhui Section (Shanxi) (Xiao *et al.* 2017b), Kouquan Section (Shanxi) (Latif *et al.* 2018), fossiliferous limestone and dolomitic limestone, respectively

at Wuhai Section (Inner Mongolia) (Riaz *et al.* 2019b), and oolitic limestone and dolomitic limestone accordingly at Kelan Section (Shanxi) (Riaz *et al.* 2019a). The deep ramp to middle ramp facies of the mentioned sections have the same lithofacies that are mainly associated with calcareous mudstone and micritic limestone (see Latif *et al.* 2018; Riaz *et al.* 2019a, b) (figure 10). The depositional trend of the upper part of the basal third-order sequence associated with glauconite-bearing ooids makes this section unique among other sections of the North China
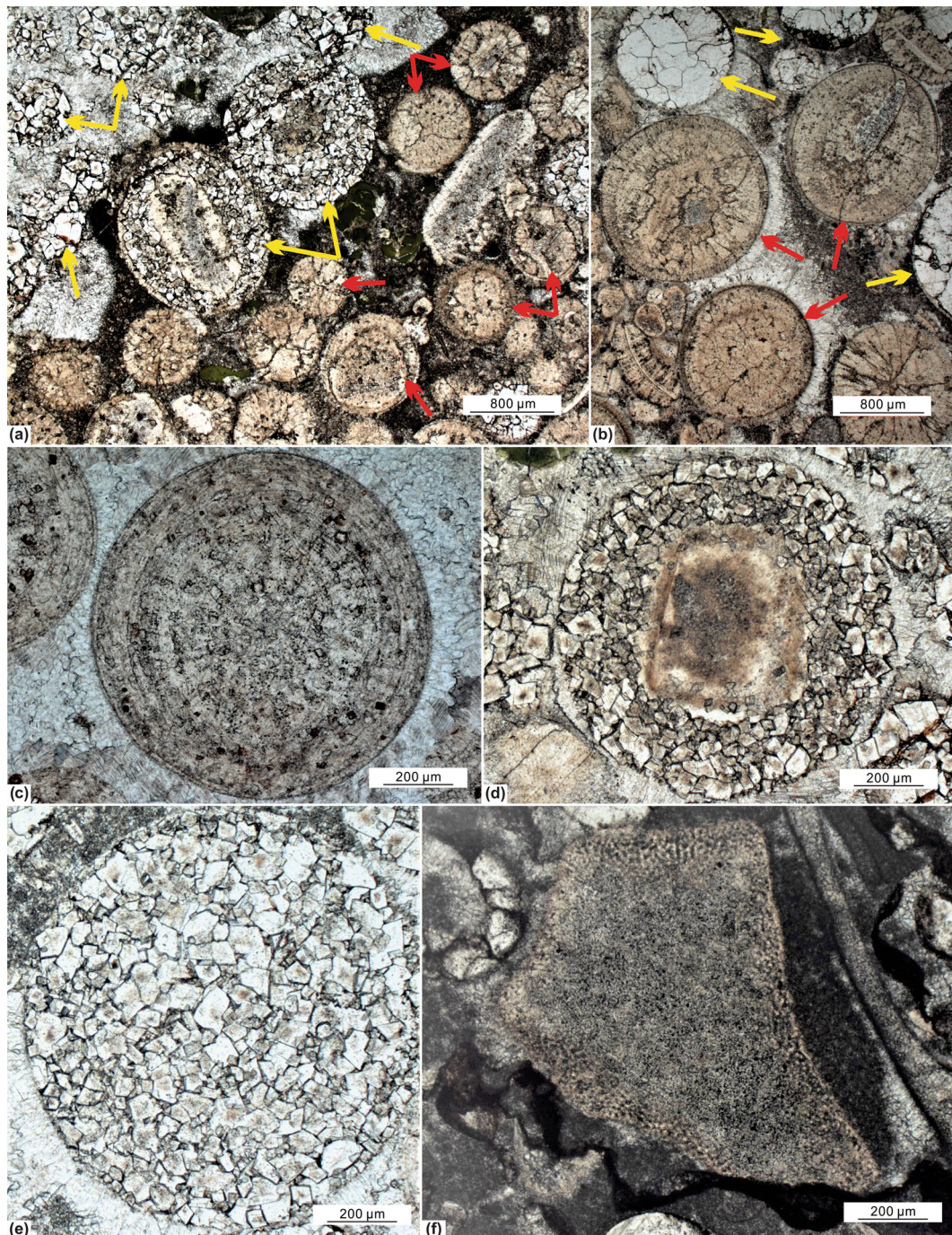
Figure 8. Photomicrographs show the carbonate constituents in the upper part of the basal Fengshan Formation. (**a**) Photograph shows the radial-concentric ooids (red arrows), and partially and completely dolomitized ooids (yellow arrows). Both types of ooids are surrounded by sparite cement, (**b**) show the radial-concentric ooids dominated with trilobites and/or brachiopods fragments in their cores (red arrows) and partially dolomitized ooids (yellow arrow), (**c, d, e**) reveal the various stages of dolomitization. The photomicrograph (c) exhibits the initial stage of dolomitization in which the cortex and core of ooids comprises calcite gradually converted into tiny crystals of dolomite. The photomicrograph (d) portrays the conversion of half portion into crystals of dolomite, whereas photomicrograph (e) clearly shows the complete conversion of calcite into dolomite, (**f**) photomicrograph displays an echinoderm fossil (large piece) and fossils of brachiopods.

Platform (figure 10) where ooids were only observed in the Miaolingian strata (Ma *et al.* 2017). Moreover, these restricted deposits in the upper part of the depositional sequence do not confirm the standard model of sequence stratigraphy of Catuneanu *et al.* (2011) where deposition usually occurs during the relative sea-level rise and erosional unconformity form during
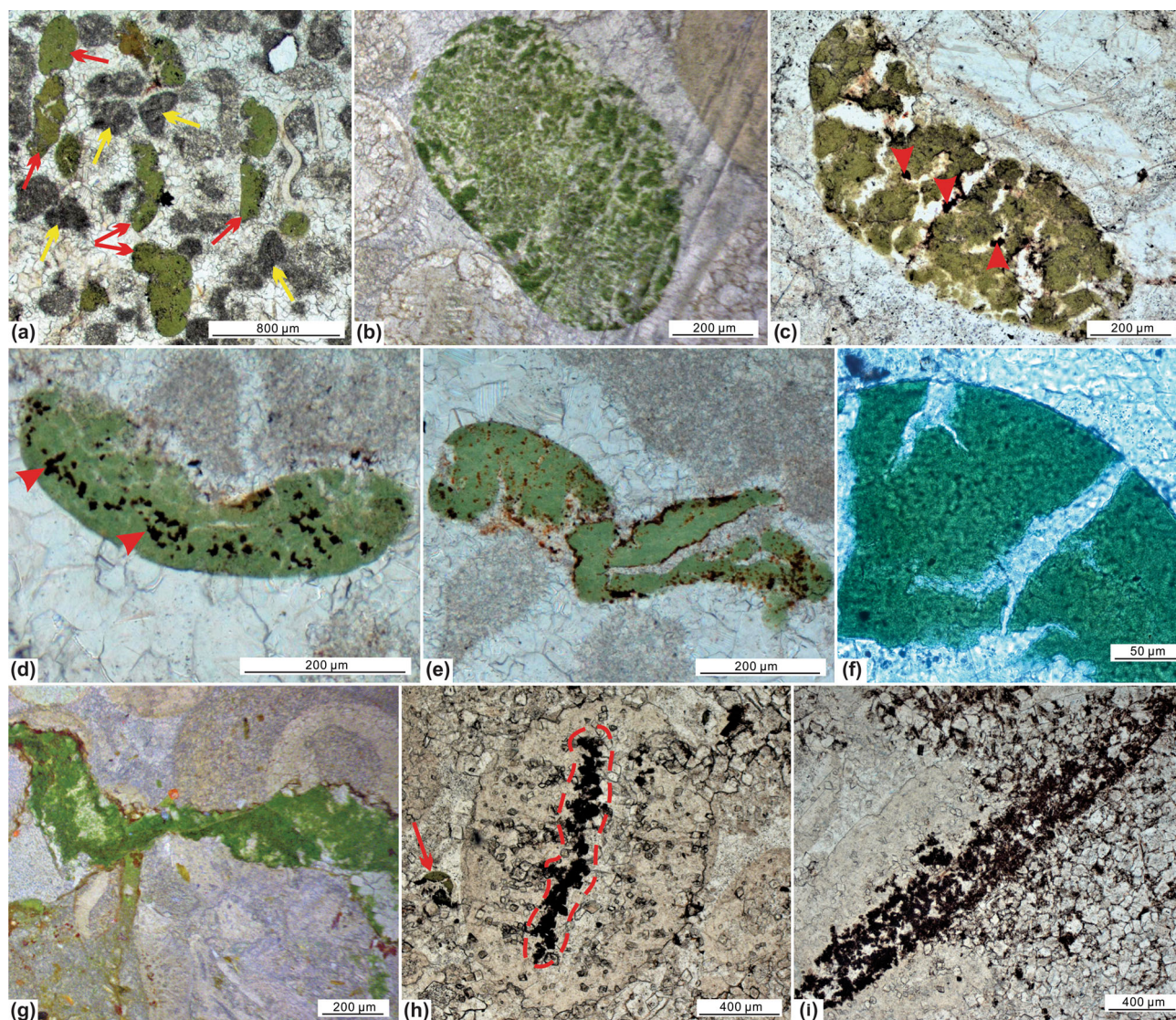
Figure 9. Photomicrographs show the non-carbonate constituents in the upper part of the basal Fengshan Formation. (**a**) Pellets of glauconite (red arrow) and patches of dark micrite (yellow arrow) surrounded by sparite cement, (**b**) pellet of glauconite and dolomitized ooids, (**c–d**) glauconitic pellets and pyrite minerals (red arrow heads) in the sparite cement, (**e**) distorted pellets of glauconite possibly due to high energy condition, (**f**) photomicrograph shows the fibro-radial rims in sparite cement partially covering the glauconitic pellets, (**g**) a band of glauconite, (**h**) pyrite mineral (dashed line) in the center of the radial-concentric ooids and a pellet of glauconite (red arrow) in the boundary of the ooids, and (**i**) a band of pyrite mineral and crystals of dolomite.

relative sea-level fall. However, these deposits follow the Schlager model (2005) of sequence stratigraphy which represents forced regressive wedge systems tract (FRWST) of Hunt and Tucker (1992), Schlager and Warrlich (2009), and Samanta *et al.* (2016) where deposition occurs during relative sea-level fall. The shallow ramp deposits associated with glauconite-bearing ooids formed during progradation instead of aggradation due to change of accommodation space and low magnitude base-level fall (i.e., shut down of carbonate factory) which cause rapid regression as described by Schlager and

Warrlich (2009). Therefore, the lower and upper boundaries of the basal third-order sequence (DS_6) of the Fengshan Formation are bounded by an abrupt transition from oolitic limestone in the upper part of the Changshan Formation to calcareous mudstone of the basal Fengshan Formation. Also, glauconite-bearing oolitic limestone in the upper part of the basal Fengshan Formation transit to the calcareous mudstone of the upper Fengshan Formation (DS_7) possibly represents the drowning type unconformity (Schlager 1999). This Type-3 unconformity is different from Type-1 and Type-2
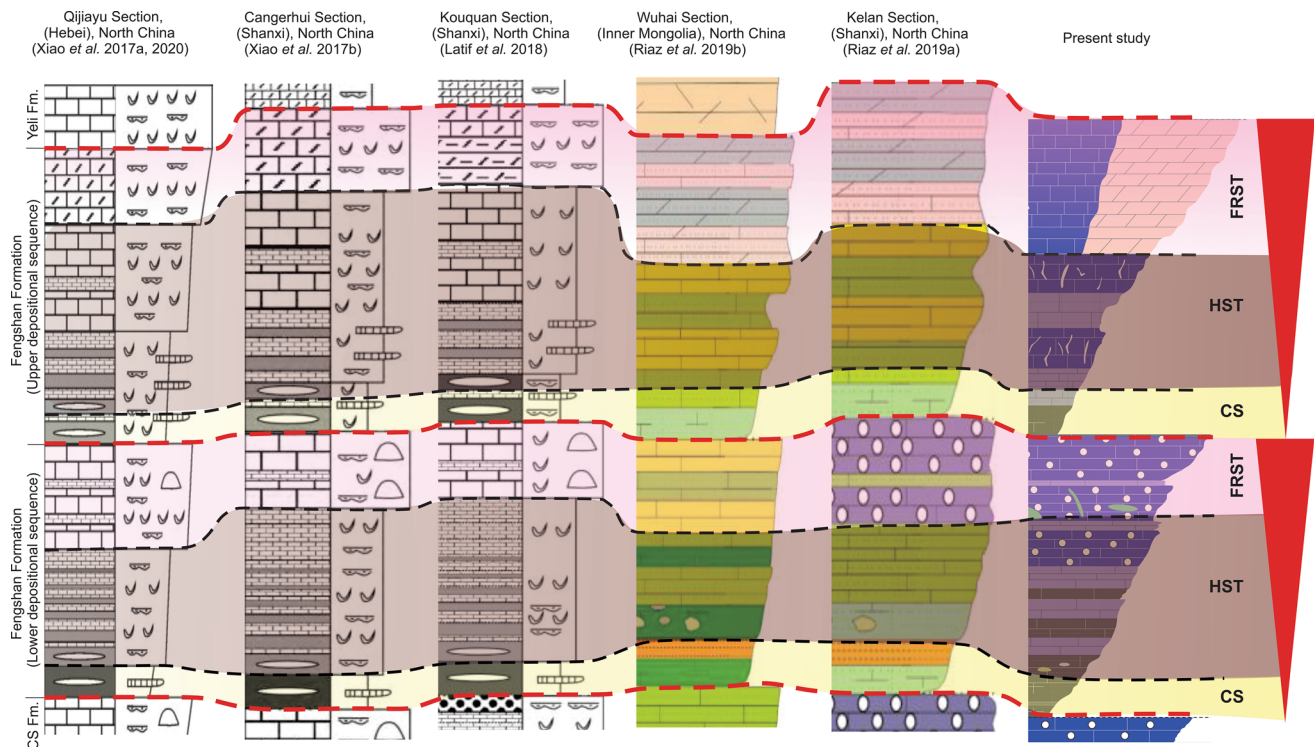
Figure 10. The comparative lithology of the Furongian Fengshan Formation exposed in various sections of the North China Platform showing the coarsening upward sequence. These lithologs also indicate the drowning events in the basal third-order sequence of the Fengshan Formation which are bounded from the lower side with fossiliferous limestone or oolitic limestone of the Changshan Formation formed during relative sea-level fall and calcareous mudstone of deep ramp facies of the basal third-order sequence of the Fengshan Formation formed during early transgression. Whereas the upper contact of the basal sequence is bounded between fossiliferous limestone or oolitic limestone of the basal third-order sequence and calcareous mudstone of deep ramp facies of the upper third-order sequence of the Fengshan Formation.

unconformity where deposition occurs during relative sea-level rise (Vail *et al.* 1977).

The XRD analysis confirms that the composition of the samples of the upper part of the basal third-order sequence of the Fengshan Formation is dominated by calcite (table 1). The observed crystals of dolomite are characteristic of an evaporitic setting during regression. Several researchers (e.g., Wang *et al.* 2018) mentioned the influence of microbe through sulfate reduction, methane-producing action, organic molecular hydrolysis in the formation of Cambrian dolomite. Moreover, the presence of quartz, potash feldspar, and kaolinite in these samples depict contributions from the terrigenous source during the limestone deposition. Also, the XRD analysis reveals fine-grained crystals of calcite with cubic morphology examined under SEM further clarifies the calcitic composition of the oolitic limestone (figure 6a, b). EDX spectrum shows the peaks of Si, K, Al, Mg, O, and Fe that confirm the presence of glauconite in the surrounding area of the ooids (figure 6d–d′).

Carbonate constituents in the DS_6 depositional sequence in the Cambrian (Furongian) Fengshan Formation at Kelan are mainly composed of radial-concentric ooids (figures 7a–c, 8a–c), and dolomitized ooids (figures 7a–b, 8a–b, d–e). The radial-concentric ooids have the same structure from the center to the outermost layers (figures 7b–c, 8c). There is no clear difference between the core and cortex. Brehm *et al.* (2003, 2006) suggested that such types of ooids are associated with nuclei of bacterial biofilm, which formed through the action of microorganisms such as cyanobacteria and sulfate-reducing bacteria. These microorganisms excrete gel-type material which makes a ring-type structure where deposition started and gradually the entire ring is replaced by the grains. There is also a possibility that these microorganisms were involved in microboring that gradually spalling and/or destroying the outer cortical layers of radial-concentric ooids (figure 8a–c) as observed in Cambrian Furongian strata of Qingshuihe Section, Inner Mongolia, China (Riaz *et al.* 2021), and Kuldhar and Keera dome carbonates of Western

India (Ahmad *et al.* 2006). The entire process occurred in shallow water rich in high nutrient supply. Moreover, these ooids are dominated by concentric ring structures and cemented by sparite indicating high-energy depositional settings (figures 7b–c, 8c). The radial-concentric ooids with the core of quartz grains or fossils of trilobite or brachiopods have a thin cortex (figures 7a, 8a–b) as compared to the radial-concentric ooids with the core of bacterial biofilm (figures 7b–c, 8c). The concentric structures of these ooids indicate their life span in a high-energy setting (Flügel 2004; Riaz *et al.* 2019a). The dolomitized ooids are cemented by sparite and are associated either with partially or completely dolomitized ooids (figures 7a–b, 8a–b, d–e). Partial dolomitization has occurred in radial-concentric ooids (figure 8c) where crystals of calcite have been gradually converted into crystals of dolomite (figure 8d). The crystals of partially dolomitized ooids show mosaic structure (variable size and shape) with defused dolomite rims around the ooids (figure 8d). The complete dolomitized ooids show a similar structure of mosaic crystals with inter-ooid high Mg-calcite cement (figures 7a, 8e). Besides ooids, bioclasts are also cemented by sparite (figures 7a, 8f) which portrays shallow shelf settings (Scholle and Ulmer-Scholle 2003). Furthermore, the presence of echinoderm fossils (figure 8f) also provides evidence of shallow, high-energy environments (Scholle and Ulmer-Scholle 2003; Riaz *et al.* 2021). Consequently, the occurrence of radial-concentric ooids (figures 7a–c, 8a–c) and dolomitized ooids (figures 7a–b, 8a–b, d–e) along with brachiopods, trilobites, and echinoderm fragments, indicate the deposition of the upper part of the DS_6 sequence of the Furongian Fengshan Formation at Kelan Section in the relatively high-energy setting.

The non-carbonate constituents such as glauconite occur in the form of pellets and fibro-radiating rims along with ooids in the upper part of the DS_6 sequence (figures 7a–c, 8a–d). The fibro-radiating rims occur around both the glauconite pellets (figure 9d) and ooids (figure 7b–c; red arrows), which represent the first post-depositional process that affected these rocks. The calcite fibro-radiating rims reflect the first stage of cementation of the carbonate grains and pellets. The fibro-radiating rims formed around a few grains suggest that the formation of rims took place before compaction. Moreover, patches of carbonate cement are covered by glauconite rims suggesting later diagenesis of the sediments. The

outward growth of glauconitic rims has not disturbed the calcite cement patches which are covered by displaced fibro-radiating rims. It means that calcite cementation of the carbonate grains post-dates deformation of the exfoliated rims. Pyrites (figure 9e–f) are possibly formed during the syn-depositional stage or eogenetic stage (i.e., Marynowski *et al.* 2008). Prior studies demonstrate close relation of pyrite formation with microbial activity particularly with sulfate-reducing bacteria (see Schieber 2002; Baumgartner *et al.* 2006; Mei *et al.* 2008; Wang *et al.* 2018; Mayayo *et al.* 2019; Xiao *et al.* 2020a). Wilkin and Barnes (1997) suggested that pyrite formation undergo four continuous processes: (1) the formation of microcrystalline nuclei of ferrous sulfide; (2) nucleate formation of pyrite (Fe_3S_4); (3) pyrite micro-crystals aggregate to form framboidal cemented texture, and (4) framboidal cemented texture transform into framboidal pyrite. The source of sulfur (S) and iron (Fe) is the most important factor in the entire process of pyrite formation (Berner and Raiswell 1983). The oxic waters comprise Fe in the form of ferric which cannot freely enter into calcite lattice (Evamy 1969); however, ferrous occurs in reducing environments and can easily enter into calcite lattice. Shallow marine water is oxic which gradually shifts into reducing conditions by percolating few centimeters below the sediment–water interface. Consequently, the non-ferroan calcite crystals mostly precipitate in the oxidizing environment at or close to the sediment–water interface. Baldermann *et al.* (2012) believe that the glauconite forming process comes to halt under anoxic conditions and when the Eh value in fecal pellets falls below the micromilieu, it results in pyrite formation. In our study, iron-sulfide precipitation was thus a limiting factor for glauconite by sequestration of Fe^{2+} comparable to many other glauconite-bearing facies. Dolomitization is the next step that occurred after glauconitization, as described by total replacement of some glauconitic pellets by dolomite and partial replacement by individual crystals of dolomite. The change of crystals from calcite to dolomite in the ooidal cortex is an obvious example of dolomite pseudomorphism. It appears neomorphism in ooids occurred earlier to dolomitization. In addition, transgression favours burial and reduction in O_2 levels and sulfidic conditions during early diagenesis. This process allows enough production of S^{2-} in pore waters from marine SO_4^{2-}, which

favours the removal of Fe^{2+} for iron-bearing mineral precipitation. The favourable physico-chemical conditions for glauconitization occur in the open marine, shelf-slope transition under sub-oxic moderately reducing conditions triggered by low sedimentation rates near the sediment–water interface. Sub-oxygenation conditions may have been provided by high energy bottom currents stirring the sediments providing appropriate conditions for glauconite authigenesis at the base of the forced regressive sequence.

Consequently, carbonate and non-carbonate constituents (figure 7a–c) in the upper part of the basal third-order depositional sequence of the Furongian Fengshan Formation (figures 2, 3b–c) at Kelan Section of the North China Platform reflect the deposition in the shallow environment during the relative sea-level fall, i.e., forced regressive systems tract. The precipitation of glauconite was closely followed by precipitation of carbonate cement as well as dissolution of aragonite constituents. The combined sedimentology and sequence stratigraphic evidences clarify that the glauconite was the earliest diagenetic event to affect these sediments and occurred essentially at the sediment–water interface within these relatively high-energy, shallow marine deposits. Therefore, deposition of glauconite in the high-energy shallow marine environment during forced regression is an alternate interpretation to the views of several researchers who suggested that glauconite is an indicator of the condensed section (CS) and HST that are deposited during relative sea-level rise (e.g., Chen 1994; Amorosi 1995, 1997, 2012; Akihisa 1998; Morad *et al.* 2000; Banerjee *et al.* 2008).

9. Conclusions

- The basal third-order depositional sequence (DS_6) of the Fengshan Formation in the Kelan Section not only shows its deposition during fluctuation of relative sea-level, but also an escape from drowning unconformity.
- The carbonate (radial concentric ooids and dolomitized ooids) and non-carbonate (glauconite and pyrite) grains in the restricted portion of the basal third-order sequence (DS_6) formed during forced regression, indicate their deposition in the high energy ramp environments.
- The glauconitization occurred in the open marine setting under sub-oxic, moderately

reducing conditions triggered by low sedimentation rates near the sediment–water interface during the forced regression.
- Iron-sulfide precipitation was a limiting factor for glauconite by sequestration of Fe^{2+}, which is comparable to many other glauconite-bearing facies worldwide.
- The deposition of glauconite-bearing ooids took place during relative sea-level fall. This inference fits well with the Schlager (2005) model of sequence stratigraphy.
- Glauconitization occurred prior to dolomitization, as indicated by partial or total replacement of glauconitic pellets by dolomite crystal(s).

Author statement

All the authors have actively participated in the preparation of this manuscript. MR and KL proposed the main concept of the manuscript and collected field and laboratory data. TZ, GMB and SG contributed to preparation, review and proof-reading of the manuscript.

References

Abdulghania A, Ghazi S, Riaz M and Zafar T 2020 Sedimentary fabrics and diagenetic features of the Late Triassic Kingriali Formation, Khisor–Marwat ranges, Pakistan; *Indian J. Geo-Mar. Sci.* **49(6)** 954–964.

Ahmad A H M, Bhat G M and Khan M H A 2006 Depositional environments and diagenesis of the Kuldhar and Keeera Dome Carbonates (Late Bathonian–Early Callovian) of Western India; *J. Asian Earth Sci.* **27(6)** 765–778.

Akihisa K 1998 Glaucony and carbonate grains as indicators of the condensed section: Omma Formation, Japan; *Sedim. Geol.* **122** 151–163.

Al-Jaroudi S S, Ul-Hamid A, Mohammed A R I and Saner S 2007 Use of X-ray powder diffraction for quantitative analysis of carbonate rock reservoir samples; *Powder Technol.* **175(3)** 115–121.

Amorosi A 1995 Glaucony and sequence stratigraphy: A conceptual framework of distribution in siliciclastic sequences; *J. Sedim. Res.* **65(4b)** 419–425.

Amorosi A 1997 Detecting compositional, spatial, and temporal attributes of glaucony: A tool for provenance research; *Sedim. Geol.* **109** 135–153.

Amorosi A 2012 The occurrence of glaucony in the stratigraphic record: Distribution patterns and sequence-stratigraphic significance; *Int. Assoc. Sedim. Spec. Publ.* **45** 37–54.

Babcock L E, Peng S and Ahlberg P 2016 Cambrian trilobite biostratigraphy and its role in developing an integrated history of the Earth system; *Lethaia* **50** 381–399.

Baldermann A, Grathoff G H and Nickel C 2012 Micromilieu-controlled glauconitization in fecal pellets at Oker (Central Germany); *Clay Miner.* **47** 513–538.

Balthasar U and Cusack M 2015 Aragonite-calcite seas – Quantifying the gray area; *Geology* **43** 99–102.

Banerjee S, Jeevankumar S and Eriksson P G 2008 Mg-rich ferric illite in marine transgressive and highstand system tracts: Examples from the Palaeoproterozoic Semri Group, central India; *Precamb. Res.* **162** 212–226.

Banerjee S, Mondal S, Chakraborty P P and Meena S S 2015 Distinctive compositional characteristics and evolutionary trend of Precambrian glaucony: Example from Bhalukona Formation, Chhattisgarh basin, India; *Precamb. Res.* **271** 33–48.

Baumgartner L K, Reid R P, Dupraz C, Decho A W, Buckley D H, Spear J R, Przekop K M and Visscher P T 2006 Sulfate reducing bacteria in microbial mats: Changing paradigms, new discoveries; *Sedim. Geol.* **185** 131–145.

Berner R A and Raiswell R 1983 Burial of organic carbon and pyrite sulfur in sediments over phanerozoic time: A new theory; *Geochim. Cosmochim. Acta* **5** 855–862.

Brehm U, Krumbein W E and Palinska K A 2003 Microbial spheres: A novel cyanobacterial-diatom symbiosis; *Naturwiss* **90** 136–140.

Brehm U, Krumbein W E and Palinska K A 2006 Biomicrospheres generate ooids in the laboratory; *Geomicrobiol. J.* **23(7)** 545–550.

Catuneanu O, Galloway W E, Kendall C G S C, Miall A D, Posamentier H W, Strasser A and Tucker M E 2011 Sequence stratigraphy: Methodology and nomenclature; *News. Stratigr.* **44(3)** 173–245.

Chen L R 1994 Evolutionary history of authigenic glauconites in early diagenesis; *Chin. Sci. Bull.* **39** 829–831 (in Chinese).

Chen J, Lee J H and Woo J 2014 Formative mechanisms, depositional processes, and geological implications of Furongian (late Cambrian) reefs in the North China Platform; *Palaeogeogr. Palaeoclimatol. Palaeoecol.* **414** 246–259.

Cordiea D R, Dornbos S Q, Marenco P J, Oji T and Gonchigdorj S 2019 Depauperate skeletonized reef-dwelling fauna of the early Cambrian: Insights from archaeocyathan reef ecosystems of western Mongolia; *Palaeogeogr. Palaeoclimatol. Palaeoecol.* **514** 206–221.

Evamy B D 1969 The precipitational environment and correlation of some calcite cements deduced from artificial staining; *J. Sedim. Petrol.* **39** 787–793.

Flügel E 2004 *Microfacies of carbonate rocks*; Springer, Berlin Heidelberg, New York, 976p.

Flügel E 2010 *Microfacies of carbonate rocks: Analysis, interpretation and application*; 2nd edn. Springer-Verlag, Berlin.

Fürsich F T, Wilmsen M, Seyed-Emami K, Cecca F and Majidifard M R 2005 The upper Shemshak Formation (Toarcian–Aalenian) of the Eastern Alborz (Iran): Biota and palaeoenvironments during a transgressive–regressive cycle; *Facies* **51** 365–384.

Gill B C, Lyons T W, Young S A, Kump L R, Knoll A H and Saltzman M R 2011 Geochemical evidence for widespread euxinia in the later Cambrian ocean; *Nature* **469** 80–83.

Haq B U and Schutter S R 2008 A chronology of Paleozoic sea-level changes; *Science* **322** 64–67.

Hunt D and Tucker M 1992 Stranded parasequence and the forced regressive wedge systems tract: Deposition during base level fall; *Sedim. Geol.* **81** 1–9.

Husson J M and Peters S E 2017 Atmospheric oxygenation driven by unsteady growth of the continental sedimentary reservoir; *Earth Planet. Sci. Lett.* **460** 68–75.

Jafarian A, Fallah-Bagtash R, Mattern F and Heubeck C 2017 Reservoir quality along a homoclinal carbonate ramp deposit: The Permian Upper Dalan Formation, South Pars Field, Persian Gulf Basin; *Mar. Petrol. Geol.* **88** 587–604.

Jafarian A, Javanbakht M, Koeshidayatullah A, Pimentel N, Salad Hersi O, Yahyaei A and Beigi M 2018 Paleoenvironmental, diagenetic, and eustatic controls on the Permo–Triassic carbonate-evaporite reservoir quality, Upper Dalan and Kangan formations, Lavan Gas Field, Zagros Basin; *Geol. J.* **53(4)** 1442–1457.

Kiessling W 2009 Geologic and biologic controls on the evolution of reefs; *Ann. Rev. Ecol. Evol. S.* **40** 173–192.

Kwon Y K, Chough S K, Choi D K and Lee D J 2006 Sequence stratigraphy of the Taebaek Group (Cambrian–Ordovician), Mideast Korea; *Sedim. Geol.* **192** 19–55.

Laakso T A and Schrag D P 2017 A theory of atmospheric oxygen; *Geobiology* **15** 366–384.

Latif K, Xiao E Z, Riaz M, Wang L, Khan M Y, Hussein A A H and Khan M U 2018 Sequence stratigraphy, sea-level changes and depositional systems in the Cambrian of the North China Platform: A case study of Kouquan section, Shanxi Province, China; *J. Him. Earth Sci.* **51(1)** 1–16.

Latif K, Xiao E Z, Riaz M and Hussein A A 2019 Calcified cyanobacteria fossils from the leiolitic bioherm in the Furongian Changshan Formation, Datong (North China Platform); *Carbonate. Evaporite.* **34** 825–843.

Lee J H, Chen J T, Choh S J, Han Z and Chuogh S K 2014 Furongian (late Cambrian) sponge-microbial mazelike reefs in the north China platform; *Palaios* **29** 27–37.

Lee J-H and Riding R 2018 Marine oxygenation, lithistid sponges, and the early history of Paleozoic skeletal reefs; *Earth-Sci. Rev.* **181** 98–121.

Ma Y S, Mei M X, Zhou R and Yang W 2017 Forming patterns for the oolitic bank within the sequence-stratigraphic framework: An example from the Cambrian Series 3 at the Xiaweidian section in the western suburb of Beijing; *Acta Petrol. Sin.* **33(4)** 1021–1036.

Marynowski L, Zatoń M and Karwowski Ł 2008 Early diagenetic conditions during formation of the Callovian (Middle Jurassic) carbonate concretions from Łuków (eastern Poland): Evidence from organic geochemistry, pyrite framboid diameters and petrographic study; *Neues Jahrb. Geol. P-A.* **247(2)** 191–208.

Mayayo M J, Yuste A, Luzon A, Corzo A, Muñoz A, Perez A and Soriano A 2019 Fe-rich microspheres pseudomorphs after pyrite framboids in Holocene fluvial deposits from NE Spain: Relationship with environmental conditions and bacterial activity; *Sedim. Geol.* **386** 103–117.

Mei M X 2010 Correlation of sequence boundaries between normal and forced regressions: The first advance in sequence stratigraphy; *J. Paleogeogr.* **12(5)** 549–564 (in Chinese with English abstract).

Mei M X 2015 Conceptual change from depositional sequences to eustatic sequences: An important development in sequence stratigraphy; *J. Stratigr.* **39(1)** 58–73 (in Chinese with English abstract).

Mei M X and Yang X D 2000 Forced regression and forced regressive wedge system tract: Revision on traditional exxon model of sequence stratigraphy; *Geol. Sci. Technol. Inf.* **19(2)** 17–21 (in Chinese with English abstract).

Mei M X, Ma Y S, Mei S L and Hu J Z 1997 Sequence-stratigraphic framework and carbonate-platform evolution for the Cambrian of the North-China Platform; *Geoscience* **11(3)** 275–282 (in Chinese with English abstract).

Mei M X, Ma Y S, Deng J and Chen H J 2005 From cycles to sequences: sequence stratigraphy and relative sea level changes for the late Cambrian of the North China Platform; *Acta Geol. Sin-Engl.* **79(3)** 372–383.

Mei M X, Yang F J, Gao J H and Meng Q F 2008 Glauconites formed in the high energy shallow-marine environment of the late Mesoproterozoic: Case study from Tieling Formation at Jixian section in Tianjin, North China; *Earth Sci. Front.* **15(4)** 146–158.

Mei M X, Latif K, Mei C J, Gao J and Meng Q F 2020a Thrombolitic clots dominated by filamentous cyanobacteria and crusts of radio-fibrous calcite in the Furongian Changshan Formation, North China; *Sedim. Geol.* **395**, https://doi.org/10.1016/j.sedgeo.2019.105540.

Mei C J, Riaz M, Long W, Latif K and Rui Z 2020b Development of Middle Cambrian leiolitic bioherms dominated by calcified microbes: A case study of the Xinji Section (North China Platform); *Mar. Microplaentol.* **157**, https://doi.org/10.1016/j.marmicro.2020.101858.

Mei M X, Riaz M, Zhang Z W, Meng Q F and Hu Y 2021 Diversified calcimicrobes in dendrolites of the Zhangxia Formation, Miaolingian Series (Middle Cambrian) of the North China craton; *J. Palaeogeogr.* **10(1)** 1–25.

Meng X H, Ge M and Tucker M E 1997 Sequence stratigraphy, sea-level changes and depositional systems in the Cambro-Ordovician of the North China carbonate platform; *Sedim. Geol.* **114(1–4)** 189–222.

Miller K G, Kominz M A, Browning J V, Wright J D, Mountain G S, Katz M E, Sugarman P J, Cramer B S, Christie-Blick N and Pekar S F 2005 The Phanerozoic record of global sea-level change; *Science* **310** 1293–1298.

Morad S, Ketzer J M and De Ros 2000 Spatial temporal distribution of diagenetic alterations in siliciclastic rocks: Implications for mass transfer in sedimentary basin; *Sedimentology* **47** 95–120.

Myrow P M, Chen J, Snyder Z, Leslie S, Fike D, Fanning M, Yuan J and Tang P 2015 Depositional history, tectonics, and provenance of the Cambrian–Ordovician succession in the western margin of the North China block; *Geol. Soc. Am. Bull.* **127** 1174–1193.

Nummedal D, Gupta S, Plint A G and Cole R D 1995 The falling stage systems tract: Definition, character and expression in several examples from the Cretaceous from the U.S. Western Interior; In: *Sedimentary responses to forced regressions* (eds) Hunt D, Gawthorpe R L and Dogherty M, Geol. Soc. London, pp. 45–48.

Peng S C, Babcock L E and Cooper R A 2012 The Cambrian Period; In: *The geologic time scale 2012* (eds) Gradstein F M, Ogg J G, Schmitz M D and Ogg G M, Elsevier, Amsterdam, vol. 19, pp. 437–488.

Pratt B R and Bordonar O L 2007 Tsunamis in a stormy sea: Middle Cambrian inner-shelf limestones of western Argentina; *J. Sedim. Res.* **77(4)** 256–262.

Pratt B R, Raviolo M M and Bordonaro O L 2012 Carbonate platform dominated by peloidal sands: Lower Ordovician La Silla Formation of the eastern Precordillera, San Juan, Argentina; *Sedimentology* **59** 843–866.

Pruss S B, Finnegan S, Fischer W W and Knoll A H 2010 Carbonates in skeleton-poor seas: New insights from Cambrian and Ordovician strata of Laurentia; *Palaios* **25(2)** 73–84.

Riaz M, Xiao E Z, Latif K and Zafar T 2019a Sequence-stratigraphic position of oolitic bank of Cambrian in North China Platform: Example from the Kelan Section of Shanxi Province; *Arab. J. Sci. Eng.* **44(1)** 391–407.

Riaz M, Latif K, Zafar T, Xiao E Z, Ghazi S, Wang L and Hussein A A A 2019b Assessment of Cambrian sequence stratigraphic style of the North China Platform exposed in Wuhai division, Inner Mongolia; *Him. Geol.* **40(1)** 92–102.

Riaz M, Zafar T, Latif K, Ghazi S and Xiao E 2020 Petrographic and rare earth elemental characteristics of Cambrian *Girvanella* oncoids exposed in the North China Platform: Constraints on forming mechanism, REE sources, and paleoenvironments; *Arab. J. Geosci.*, https://doi.org/10.1007/s12517-020-05750-8.

Riaz M, Zafar T, Latif K, Ghazi S and Xiao E Z 2021 Cambrian ooids, their genesis and relationship to sea-level rise and fall: A case study of the Qingshuihe section, Inner Mongolia, China; *Stratigraphy* **18(2)** 139–151.

Riding R 2000 Microbial carbonates: The geological record of calcified bacterial-algal mats and biofilms; *Sedimentology* **47**(Suppl. 1) 179–214.

Riding R 2011a Microbialites, stromatolites, and thrombolites; In: *Encyclopedia of Geobiology* (eds) Reitner J and Thiel V, Springer, Berlin, pp. 635–654.

Riding R 2011b Calcified cyanobacteria; In: *Encyclopedia of Geobiology* (eds) Reitner J and Thiel V, Springer-Verlag, Berlin, Heidelberg, pp. 211–223.

Rowland S M and Shapiro R S 2002 Reef patterns and environmental influences in the Cambrian and earliest Ordovician; In: *Phanerozoic reef patterns* (eds) Kiessling W, Flügel E and Golonka J, *SEPM Spec. Publ., Tulsa* **72** 95–128.

Saltzman M R, Edwards C T, Adrain J M and Westrop S R 2015 Persistent oceanic anoxia and elevated extinction rates separate the Cambrian and Ordovician radiations; *Geology* **43** 807–810.

Samanta P, Mukhopadhyay S and Eriksson P G 2016 Forced regressive wedge in the Mesoproterozoic Koldaha shale, Vindhyan basin, Son Valley, central India; *Mar. Petrol. Geol.* **71** 329–343.

Schieber J 2002 Sedimentary pyrite: A window into the microbial past; *Geology* **30** 531–534.

Schlager W 1999 Type 3 sequence boundaries; In: *Advances in carbonate sequence stratigraphy: Application to reservoirs, outcrop, and models* (eds) Harris P M, Saller A H and Simo J A, *SEPM Spec. Publ.* **63** 35–46.

Schlager W 2005 Carbonate sedimentology and sequence stratigraphy; *SEPM Sedimentol. Paleontol.* **8** 1–200.

Schlager W and Warrlich G 2009 Record of sea-level fall in tropical carbonates; *Basin Res.* **21(2)** 209–224.

Scholle P A and Ulmer-Scholle D S 2003 A color guide to the petrography of carbonate rocks: Grains, textures, porosity, diagenesis; *AAPG Memoir* **77** 461.

Tucker M and Garland J 2010 High-frequency cycles and their sequence stratigraphic context: Orbital forcing and tectonic controls on Devonian cyclicity Belgium; *Geol. Belg.* **13(3)** 213–240.

Vail P R, Mitchum R M Jr and Thompson S III 1977 Seismic stratigraphy and global changes of sea level, part four: global cycles of relative changes of sea level; *AAPG Memoir* **26** 83–98.

Wang H, Xiao E Z, Li Y, Latif K and Riaz M 2018 Study advances and existed problem for the forming mechanism of the microbial dolomite; *Int. J. Oil Gas Coal Eng.* **6(6)** 126–133.

Whisonant R C 1987 Palaeocurrent and petrographic analysis of imbricate intraclasts in shallow-marine carbonates: Upper Cambrian, southwestern Virginia; *J. Sedim. Petrol.* **57** 983–994.

Wilkin R T and Barnes H L 1997 Formation processes of framboidal pyrite; *Geochim. Cosmochim. Acta* **2** 323–339.

Wotte T, Álvaro J J, Shields G A, Brown B, Brasier M D and Veizer J 2007 C-, O- and Sr-isotope stratigraphy across the Lower-Middle Cambrian transition of the Cantabrian Zone (Spain) and the Montagne Noire (France), West Gondwana; *Palaeogeogr. Palaeoclimatol. Palaeoecol.* **256** 47–70.

Xiao E Z, Qin Y, Riaz M, Latif K, Yao L and Wang H 2017a Sequence stratigraphy division of Cambrian in northeast area of Lvliang Mountain: A case study of the Cangerhui section in Wenshui City; *J. Northeast Pet. Univ.* **41(5)** 43–53 (in Chinese with English abstract).

Xiao E Z, Sui M, Qing Y, Latif K, Riaz M and Wang H 2017b Cambrian sequence stratigraphic division for Qijiayu section in Hebei Laiyuan; *Pet. Geol. Oilfield Dev. Daqing* **36(6)** 16–25 (in Chinese with English abstract).

Xiao E Z, Latif K, Riaz M, Qin Y L and Wang H 2018 Calcified microorganisms bloom in Furongian of the North China Platform: Evidence from microbialitic–bioherm in Qijiayu Section, Hebei; *Open Geosci.* **10** 250–260.

Xiao E Z, Latif K and Riaz M 2020a The genetic implications of microbial fossils for microbial carbonate: An example of Cambrian in North China Platform; *Him. Geol.* **41(2)** 183–194.

Xiao E Z, Zafar T, Latif K, Riaz M and Lu Y 2020b Geochemical and petrographic analyses of the Cambrian oncoids of the North China Platform: Implications for their paleogeography and paleoenvironment; *Arab. J. Sci. Eng.* **45(1)** 307–325.

Xiao E Z, Jiang S, Zafar T, Riaz M, Latif K, Setoyama E, Wang H and Xin H 2021a Sequence stratigraphic and petrological analyses of the Cambrian oncoids exposed in the Liaoning Province, North China Platform; *Austr. J. Earth Sci.* **68(6)** 868–885.

Xiao E Z, Riaz M, Zafar T and Latif K 2021b Cambrian marine radial Cerebroid ooids: Participatory products of microbial processes; *Geol. J.*, https://doi.org/10.1002/gj.4203.

Corresponding editor: Joydip Mukhopadhyay